

# Numerical simulation and experimental investigation of bending deformation mechanism during post-rolling air-cooling of AH36 L-beam

Xianming Zhao (✉ [prof\\_zhaoxm@163.com](mailto:prof_zhaoxm@163.com))

Northeastern University <https://orcid.org/0000-0001-6329-8957>

Jie Li

Northeastern University

Dezhi Li

Northeastern University

Yang Yang

Northeastern University

---

## Research Article

**Keywords:** Numerical simulation, L-beam, Bending deformation, Phase transformation, Cooling shrinkage strain, Stress

**Posted Date:** April 26th, 2022

**DOI:** <https://doi.org/10.21203/rs.3.rs-1564469/v1>

**License:**   This work is licensed under a Creative Commons Attribution 4.0 International License.

[Read Full License](#)

---

# **Numerical simulation and experimental investigation of bending deformation mechanism during post-rolling air-cooling of AH36 L-beam**

Jie Li, Xianming Zhao\*, Dezhi Li, Yang Yang

The State Key Laboratory of Rolling and Automation, Northeastern University,  
Shenyang 110819, PR China

**Corresponding author:** Xianming Zhao; **Email:** prof\_zhaoxm@163.com.

## **ABSTRACT**

L-beam is a widely used structural steel. The study of the three-stage bending deformation mechanism of L-beam under non-uniform cooling conditions is of great significance to ensure the quality, improve the yield of steel and reduce the stress level in the finished L-beam. However, it is difficult to investigate experimentally due to the high temperature and simultaneous changes of various influencing factors during the air-cooling process of the L-beam. Numerical simulation provides a convenient and feasible method to study the bending deformation mechanism of the L-beam. In order to investigate the effects of phase transformation and cooling shrinkage on the bending deformation of AH36 L-beam, a three-dimensional thermal-metallurgical-mechanical coupling model was established in this study, the microstructure distribution, hardness, strain, deformation status and stress during the air-cooling of L-beam were calculated. The results show that the microstructure distribution and deformation condition calculated by the model considering the phase transformation effect better agree with the actual situation. Considering the phase change effect is the key to improving the accuracy of the model calculation. The change of heat transfer coefficient caused by phase transformation affects the deformation tendency of the L-beam, while the transformation strain affects the amount of deformation of the L-beam. The alternating changes in the sum of the transformation strain and the cooling shrinkage strain result in a change of stress state which ultimately also results in a three-stage bending deformation of the L-beam.

**Keywords:** Numerical simulation, L-beam, Bending deformation, Phase transformation, Cooling shrinkage strain, Stress

## **1. Introduction**

There is a wide range of applications for L-beam, which is not only used in large ship frame structures but also in marine engineering structures and demanding building engineering structures. L-beam is mainly produced by hot rolling. Most manufacturers use air-cooling after rolling to produce L-beam due to the limitation of production equipment and production cost. L-beam has serious asymmetry in cross-section (different length and thickness on both sides), which inevitably results in non-uniform cooling under air-cooling conditions, which leads to non-uniform phase transformation expansion and cooling contraction of the metal. The non-uniform expansion and contraction of the metal generates huge internal stress [1] and also causes bending deformation of the L-beam during cooling. As cooling proceeds, the bending of the L-beam exists in three stages, first bending toward the short edge after final rolling, then bending toward the long edge, and finally bending toward the short edge again. The bending deformation of the L-beam seriously affects the yield rate of the beam. If the internal stress cannot be removed at the end of cooling, residual stress will be formed inside the L-beam. The bending deformation of the L-beam can be corrected by the straightening process, but the stress level inside the section after straightening is not significantly reduced due to the stress inheritance behavior [2,3]. Residual stress is beneficial only in a few cases, the bearing surface compressive stresses can improve wear resistance [4]. In structural steels such as L-beam, the presence of residual stress can have a negative impact on reducing the stiffness of the structure, negatively affecting its load-bearing capacity and stress corrosion capacity, and seriously affecting the safety of the structure [5-8]. Therefore, the study of the deformation mechanism during the air-cooling process of the L-beam is not only important for improving the yield rate of the L-beam but also can provide guidance for reducing the initial stress level of the L-beam before straightening.

The complex deformation during the cooling process of the L-beam mainly

originates from the phase transformation effect of the material and the cooling shrinkage effect. However, the specific effects of both on the three-stage deformation of the L-beam have yet to be determined. In the cooling process of L-beam, the contraction and phase transformation of steel occur simultaneously, and it is difficult to quantitatively analyze the effects of each factor on the stress formation and bending deformation of the process by purely experimental methods, whereas numerical methods do not have the above limitations and provide a low-cost, safe and fast tool [9-11]. ABAQUS is a large commercial finite element software and provides a wide range of user subroutines, which can be used by the users to realize the relevant models according to their needs [12-14]. Many researchers have used finite element software to develop three-dimensional coupled thermal-metallurgical-mechanical models to investigate related problems. Simsir C et al [15] developed a 3D finite element model using Marc software subroutine to predict the temperature, microstructure and internal stress in steel structural members during quenching in order to obtain the desired microstructure and residual stress distribution while having less deformation. Hamelin et al [16] used the ABAQUS user subroutine to develop a numerical model that can accurately predict the ferrite phase distribution and residual stress field distribution in ferritic steels, and the results showed that considering the phase transformation kinetics can significantly improve the model accuracy. Lee et al [17] established a sequentially coupled three-dimensional thermal-metallurgical-mechanical finite element model to predict the axial and circumferential residual stress generated by welding of high-strength carbon steel pipes, and the results of the study showed that the volume change due to phase transformation affected the model accuracy. Dean et al [18, 19] developed a set of thermal-metallurgical-mechanical computational models based on ABAQUS software to simulate the welding temperature field, microstructure and residual stress of multi-pass welded 2.25Cr-1Mo steel tubes. The results also show that the phase transformation strain has a significant effect on the residual stresses. Phase change strain not only changes the magnitude of the residual stress but also changes the tensile and compressive nature of the stress. Kumar et al [20] established a finite element-based coupled thermal-

metallurgical-mechanical sequence model in order to overcome the undesirable effects of residual stress and deformations in welded structures and found that phase transformation has a significant effect on the generation of residual stress and deformation. The above studies show that phase transformation effects play an important role in the evolution of deformation and stress generation, but no similar studies have been conducted for complex section steel such as hot-rolled L-beam.

In this study, a three-dimensional coupled thermo-metallurgical-mechanical model that can predict the temperature, microstructure, hardness, deformation, strain and stress of L-beam was developed in order to investigate the complex deformation mechanism of AH36 L-beam during post-rolling air cooling. The model is built based on ABAQUS software and USDFLD, UEXPAN, and HETVAL subroutines. The microstructure field is first calculated based on the temperature field data using the USDFLD subroutine. The calculation results of the microstructure fields are passed to the UEXPAN subroutine to calculate the phase change expansion, which is incorporated into the mechanical analysis. The HETVAL subroutine is used to calculate the latent heat of phase transformation of the L-beam during the air-cooling process. The accuracy of the model is verified by comparing the calculated deformation, phase change results and residual stress results with the actual production results and the validation results. Finally, the specific roles of phase transformation and cooling shrinkage effects in the process of complex deformation of L-beam are discussed.

## **2. Experiment**

The chemical composition of the investigated AH36 steel is shown in Table 1. The high-temperature mechanical properties of AH36 were obtained by a universal testing machine (CMT5105) at 300°C, 450°C, 550°C, 650°C, 750°C, and 900°C. The true stress-strain data for AH36 are shown in Table 2. The phase transformation temperature of AH36 was determined by using the Formastor-FII. Fig. 1 shows the thermal expansion curves of AH36 steel. The phase transformation temperature interval of AH36 steel is 565 °C ~770 °C. The observation of the metallographic

structure was carried out with an OM metallographic microscope. AH36 steel mainly contained ferrite and pearlite under air-cooled conditions, as shown in Fig. 2. The hardness was measured by using the FM-700 microhardness tester. In this study, the tensile specimens and the specimens of the phase transition instrument experiment were taken from L-beam with a specification of L 200mm×90mm×9mm×14mm. The temperature of the L-beam after rolling was captured using the FLIR infrared thermal imager.

**Table 1**

Chemical composition (in wt%) of AH36.

C	Si	Mn	P	S	Cu	Cr	Ni	Nb	V	Ti	Mo	Al
0.152	0.334	1.27	0.03	0.01	0.052	0.037	0.038	0.017	<0.001	0.002	0.0051	0.026

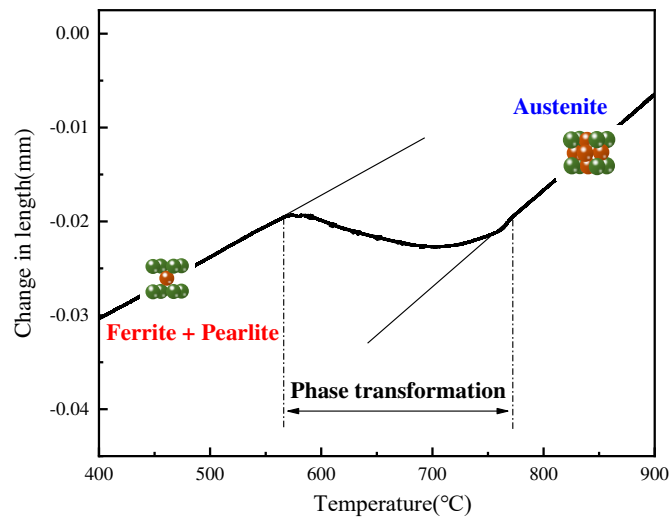


**Fig. 1.** The expansion curve of AH36 steel under air-cooling conditions.

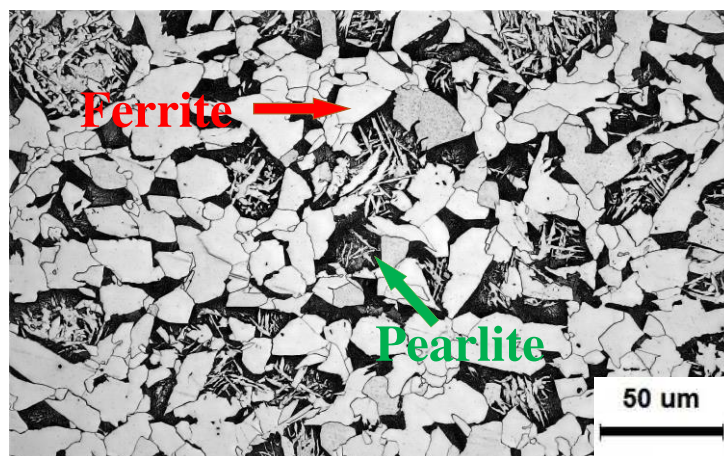


**Fig. 2.** Microstructure of AH36 steel.

**Table 2**

True stress (MPa) and true strain of AH36 steel at elevated temperatures.

300°C		450°C		550°C		650°C		750°C		900°C	
True stress	True strain										
347.33	0	271.61	0	267.26	0	145.62	0	73.83	0	45.07	0
555.6	0.043	493.52	0.047	326.23	0.0164	153.33	0.0039	82.58	0.0487	54.29	0.0305
671.69	0.94	545.96	0.093	338.26	0.0253	158.89	0.0092	84.03	0.0807	56.76	0.0539
709.97	0.127	560.39	0.126	346.17	0.0384	161.11	0.0181	85.31	0.1199	58.45	0.0856
735.17	0.169	565.54	0.167	349.7	0.055	161.7	0.0288	86.122	0.179	59.44	0.1227

### 3. Model description

#### 3.1 Thermal analysis

The degree of accuracy of the temperature field calculation has a large impact on the calculation of the phase transformation and stress field. The initial temperature field of the L-beam was obtained by fitting the actual data measured by the infrared thermal imaging camera. The infrared thermal imaging camera photographs as shown in Fig. 3.

The temperature distribution across the L-beam during subsequent cooling was calculated by means of the nonlinear transient heat transfer equation [21,22]:

$$\rho c \frac{\partial T}{\partial t} = \lambda \left( \frac{\partial^2 T}{\partial x^2} + \frac{\partial^2 T}{\partial y^2} + \frac{\partial^2 T}{\partial z^2} \right) + \Phi \quad (1)$$

where  $T$  is the temperature ( $^{\circ}\text{C}$ ),  $\lambda$  is the thermal conductivity ( $\text{W}\cdot\text{m}^{-1}\cdot\text{K}^{-1}$ ),  $\rho$  is the density of AH36 steel ( $\text{kg}\cdot\text{m}^{-3}$ ),  $c$  is the specific heat ( $\text{J}\cdot\text{kg}^{-1}\cdot\text{K}^{-1}$ ),  $\Phi$  is internal heat source intensity ( $\text{W}\cdot\text{m}^{-3}$ ),  $t$  is the time (s).

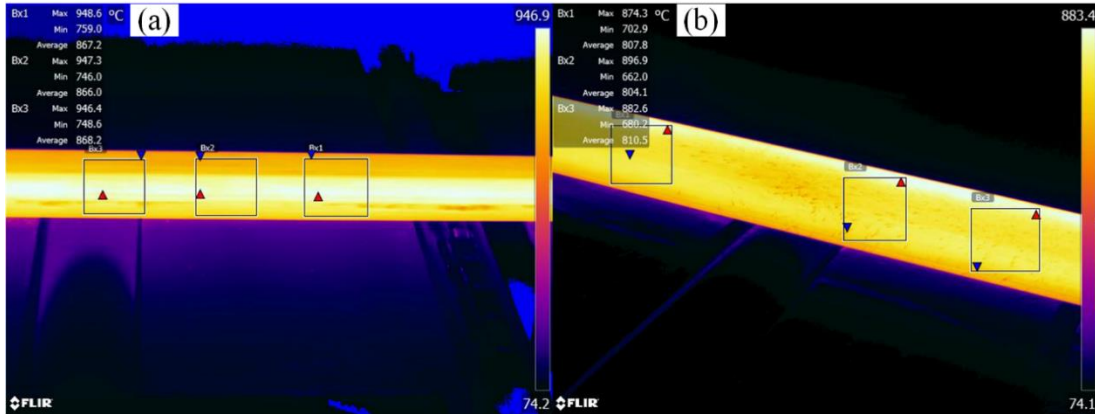


**Fig. 3.** Infrared thermal imaging camera photographs: (a) Photograph of the short edge of the L-beam; (b) Photograph of the long edge of the L-beam.

The heat transfer method in the air-cooling process of L-beam after rolling is mainly convection and radiation. The heat loss caused by natural convection and radiation as boundary conditions is defined by Eq. (2) and Eq. (3), respectively.

$$q_c = h(T_s - T_w) \quad (2)$$

$$q_r = \varepsilon\sigma \left[ (T_s - T_{abs})^4 - (T_w - T_{abs})^4 \right] \quad (3)$$

where  $h$  is the heat transfer coefficient ( $\text{W}/(\text{m}^2 \cdot ^\circ\text{C})$ ),  $T_s$  is the current temperature ( $^\circ\text{C}$ ),  $T_w$  is the ambient temperature ( $^\circ\text{C}$ ),  $T_{abs}$  is the absolute zero temperature ( $^\circ\text{C}$ ),  $\varepsilon$  is the emissivity,  $\sigma$  is the Stefan-Boltzmann constant ( $5.67 \times 10^{-8} \text{ W} \cdot \text{K}^{-4} \cdot \text{m}^{-2}$ ).

The heat transfer coefficient under air-cooled conditions is calculated by Eq. (4).

$$h = 2.25(T_s - T_c)^{0.25} + 4.6 \times 10^{-8} (T_s^2 + T_c^2)(T_s + T_c) \quad (4)$$

where  $T_s$  is the steel surface temperature (K),  $T_c$  is the external ambient temperature (K).

The internal heat source intensity in this investigation is the latent heat of phase change. The data in Tables 3-5 were cited from the literature of Bailey and de Oleivera [23,24]. The enthalpy of phase transformation is shown in Table 2. The latent heat is defined as [25]:

$$\dot{Q} = \sum_k \Delta H_k \frac{\Delta \zeta_k}{\Delta t} \quad (5)$$

where  $\Delta H_k$  is the enthalpy of phase transformation  $\text{k}(\text{J}/\text{m}^3)$ ,  $\zeta_k$  is the proportion of the phase  $k$ ,  $\Delta t$  is the time increment.

**Table 3**

Enthalpy of phase transformation.

Phase transformation	$\Delta H_k (\text{J}/\text{m}^3)$
Austenite to pearlite	$1.56 \times 10^9 - 1.50 \times 10^6 T$
Austenite to ferrite	$1.082 \times 10^2 - 0.162(T+273) + 1.118 \times 10^{-4}(T+273)^2 - 3.0 \times 10^{-8}(T+273)^3 - 3.501 \times 10^{-4}(T+273)^{-1}$

### 3.2 Metallurgical analysis

In this study, the material of L-beam is AH36. The microstructure distribution of the L-beam is obtained from the calculated history of the temperature field by means of the phase transformation model. The diffusion-type phase transformation occurred during the air-cooling process of AH36 L-beam after rolling. Generally, the Johnson-

Mehl-Avrami-Kolmogorov equations were used for the diffusion-type transformations [26,27]. Based on the modified Avrami equation, the kinetic model of ferrite growth was established using the additivity rule, and the isothermal ferrite phase transformation model can be expressed as [28,29]:

$$\frac{\zeta_{\alpha}}{\zeta_{\alpha}^E} = 1 - \exp\left(1 - \frac{kt^n}{(d_{eff}^{\gamma})^m}\right) \quad (6)$$

where  $\zeta_{\alpha}^E$  is the fraction of ferrite phase at equilibrium,  $k$  is the temperature-related parameter,  $d_{eff}^{\gamma}$  is equivalent austenite grain size,  $n$  is Avrami index,  $m$  is grain size index.

Eq. (7) was derived from Eq. (6), in which the fraction of ferrite for continuous cooling transformation during air-cooling can be calculated.

$$\frac{d\zeta_{\alpha}}{dt} = n\zeta_{\alpha}^E \left(\frac{k}{(d_{eff}^{\gamma})^m}\right)^{1/n} \cdot \left(-\ln\left(1 - \frac{\zeta_{\alpha}}{\zeta_{\alpha}^E}\right)\right)^{(n-1)/n} \cdot \left(1 - \frac{\zeta_{\alpha}}{\zeta_{\alpha}^E}\right) \quad (7)$$

The pearlite phase transformation can be calculated by Eq. (8).

$$\frac{d\zeta_P}{dt} = k_1 S_{\gamma} G_p (1 - \zeta_P - \zeta_{\alpha}) \quad (8)$$

where  $\zeta_P$  is the Phase fraction of pearlite,  $k_1$  is the material-related parameter,  $G_p$  is the growth rate of pearlite,  $S_{\gamma}$  is equivalent to grain surface area of austenite phase per unit volume.

### 3.3 Hardness calculation

The hardness distribution of the L-beam was calculated using the rule of mixtures [16, 30]:

$$Hv = \zeta_M Hv_M + \zeta_B Hv_B + (\zeta_F + \zeta_P) Hv_{F+P} \quad (9)$$

where  $Hv_M$  represents the hardness (in Vickers);  $\zeta_M$ ,  $\zeta_B$ ,  $\zeta_F$ ,  $\zeta_P$  represent the volume fraction of martensite, bainite, ferrite and pearlite, respectively;  $Hv_M$ ,  $Hv_B$ ,  $Hv_{F+P}$  represent the predicted hardness values for

martensite, bainite and the mixture of ferrite and pearlite, respectively.

$$Hv_M = 127 + 949C + 27Si + 11Mn + 8Ni + 16Cr + 21\log(V_r) \quad (10)$$

$$Hv_B = -323 + 185C + 330Si + 153Mn + 65Ni + 144Cr + 191Mo + (89 + 53C - 55Si - 22Mn - 10Ni - 20Cr - 33Mo)\log(V_r) \quad (11)$$

$$Hv_{F+P} = 42 + 223C + 53Si + 30Mn + 12.6Ni + 7Cr + 19Mo + (10 - 19Si + 4Ni + 8Cr + 130V)\log(V_r) \quad (12)$$

where the variable  $V_r$  represents the cooling rate ( $^{\circ}\text{C}/\text{h}$ ) that is present in the material at  $700\text{ }^{\circ}\text{C}$ ; Alloying elements (C, Si, Mn, etc.) are given in wt.%.

### 3.4 Mechanical analysis

The total strain increments generated during cooling after rolling can be decomposed as follows [31, 32]:

$$d\varepsilon_{ij} = d\varepsilon_{ij}^e + d\varepsilon_{ij}^p + d\varepsilon_{ij}^{th} + d\varepsilon_{ij}^{tr} \quad (13)$$

where  $d\varepsilon_{ij}^e$  is the increment of elastic strain,  $d\varepsilon_{ij}^p$  is the plastic strain,  $d\varepsilon_{ij}^{th}$  is the thermal strain,  $d\varepsilon_{ij}^{tr}$  is the transformation strain. TRIP was not considered in this investigation.

The elastic strain is calculated by Hook's law:

$$d\varepsilon_{ij}^e = \frac{1}{E} \left[ (1+\nu)d\sigma_{ij} - \nu d\sigma_{kk} \delta_{ij} \right] \quad (14)$$

where  $E$  is Young's modulus,  $\nu$  is the Poisson's ratio,  $\sigma_{ij}$  is the stress component,  $\sigma_{kk}$  is the mean stress,  $\delta_{ij}$  is the Kronecker delta.

The increment of plastic strain can be written as below:

$$d\varepsilon_{ij}^p = \frac{3}{2} dp \frac{\sigma'_{ij}}{\sigma_e} \quad (15)$$

where  $\sigma_e$  is the equivalent stress,  $\sigma'$  is the deviatoric stress,  $p$  is the equivalent plastic strain.

A variety of material parameters are significantly affected during the cooling of the L-beam due to the occurrence of phase change. Therefore,

the linear mix rule was considered to resolve the issue in this study. The thermal strain when different phases coexist is expressed as follows [33]:

$$d\varepsilon_{ij}^{th} = \sum_k \alpha_k d\zeta_k dT \delta_{ij} \quad (16)$$

where  $\alpha_k$  is the thermal expansion coefficient of the phase k,  $\zeta_k$  is the proportion of the phase k,  $dT$  is the increment of temperature,  $k = 1,2,3$ , represents ferrite, pearlite, austenite respectively. The thermal expansion coefficients of different phases are shown in Table 4.

The microstructure will change in volume due to the volume difference between the new phase and the parent phase when the phase change occurs. The strain due to the volume difference between the new phase and the parent phase is the transformation strain. The transformation strain is defined as [34]:

$$d\varepsilon_{ij}^{tr} = \sum_k \xi_k d\zeta_k \delta_{ij} \quad (17)$$

where  $\xi_k$  is the transformation strain coefficient of the phase k. Table 5 shows the transformation strain coefficient.

**Table 4**

Expansion coefficient of each phase.

Phase	$\alpha(1/^\circ\text{C})$
Ferrite	$1.61 \times 10^{-5}$
Pearlite	$1.53 \times 10^{-5}$
Austenite	$2.20 \times 10^{-5}$

**Table 5**

Transformation strain coefficient

Phase transformation	$\xi_k = \Delta V / 3V (\%)$
Austenite to ferrite	0.110
Austenite to pearlite	0.126

### 3.5 The thermo-metallurgical-mechanical model implemented in ABAQUS

The simulation was carried out in ABAQUS. A three-dimensional finite element model of L-beam was established by ABAQUS/Standard to simulate its bending deformation during air-cooling. The mesh cell type of

the model was chosen as C3D8T, and the total number of elements and nodes was 288,702 and 363,475, respectively. Fig. 4 shows the cross-sectional dimensions and finite element model of the L-beam. The relevant thermal physical parameters and thermal-mechanical properties were calculated by Jmat-Pro software as shown in Fig. 5. The cooling medium is air and the air-cooled heat transfer coefficient is calculated by Eq. (4).

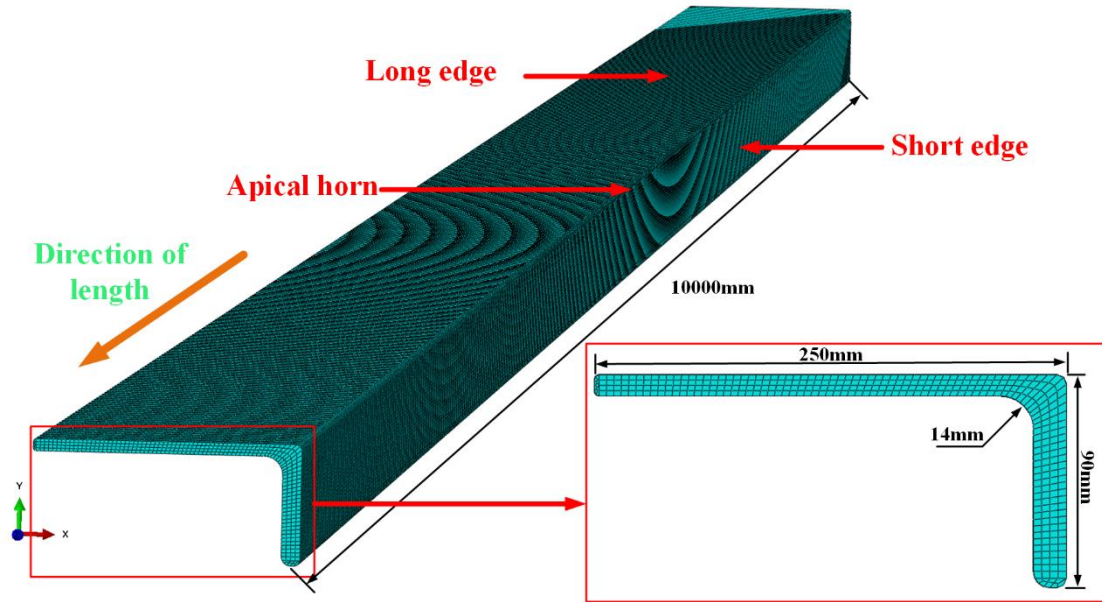


**Fig. 4.** Schematic diagram of cross-sectional dimensions and finite element model of L-beam.

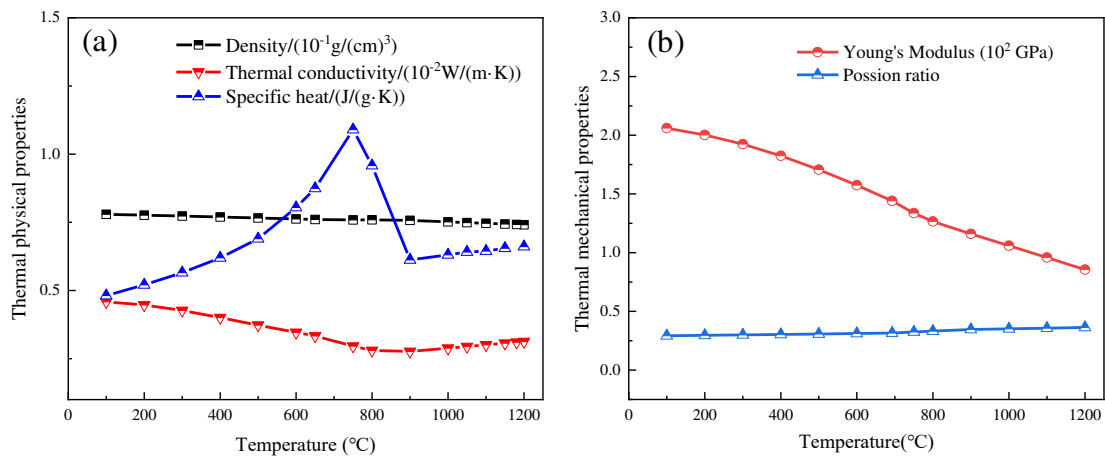


**Fig. 5.** Material properties of AH36 steel dependent on the temperature: (a) Thermal physical properties; (b) Thermal mechanical properties.

Some assumptions and simplifications in this study deserve to be invoked to reduce the difficulty of the calculations, but also to reflect a large extent of the real post-rolling air-cooling process of L-beam, which

are summarized as:

(1) Since the hot-rolled L-beam does not stay long in the transfer roller conveyor and has a small contact area with the cold bed after entering the cold bed. The heat transfer between the L-beam and the roller conveyor as well as the cold bed was ignored in this study.

(2) In the rolling process of the L-beam internal stress will be generated, at this time the L-beam is at high temperature and low strength, the bending deformation does not occur in the process interval, it can be considered that the stress is small and does not trigger bending deformations in the L-beam, so the stress generated by the rolling process can be ignored. Stress is calculated from the air-cooling process of the L-beam.

The post-rolling air-cooling process of L-beam is a complex process that involves temperature change, phase transformation, strain and stress evolution. Many user subroutines furnish an extremely powerful and flexible tool for analysis are provided in ABAQUS. In this study, the thermo-metallurgical-mechanical model coupling diagram is shown in Fig. 6. ABAQUS user subroutines USDFLD, UEXPAN, and HETVAL were used to develop the program and implement them by FORTRAN language. The metallurgical model is programmed via the user subroutine USDFLD. Based on the temperature history, the microstructure evolution and hardness of the L-beam under air-cooling conditions can be calculated by using this subroutine USDFLD. Latent heat is also generated during the phase transformation process. The latent heat of phase transformation is calculated utilizing the subroutine HETVAL. The transformation strain is quantified by using the subroutine UEXPAN. The sum of the thermal strain and the transformation strain is recorded as the new thermal strain using the subroutine UEXPAN for calculation, as shown in Eq. (18)-(19). In this way, the transformation strain was introduced into the calculation of the stress. SDVs are the state variables that can be updated in a

subroutine and passed into other user subroutines. The calculation flow of the subroutines is shown in Fig. 7.

$$d\varepsilon_{ij}^{th'} = d\varepsilon_{ij}^{th} + d\varepsilon_{ij}^{tr} \quad (18)$$

$$d\varepsilon_{ij} = d\varepsilon_{ij}^e + d\varepsilon_{ij}^p + d\varepsilon_{ij}^{th'} \quad (19)$$

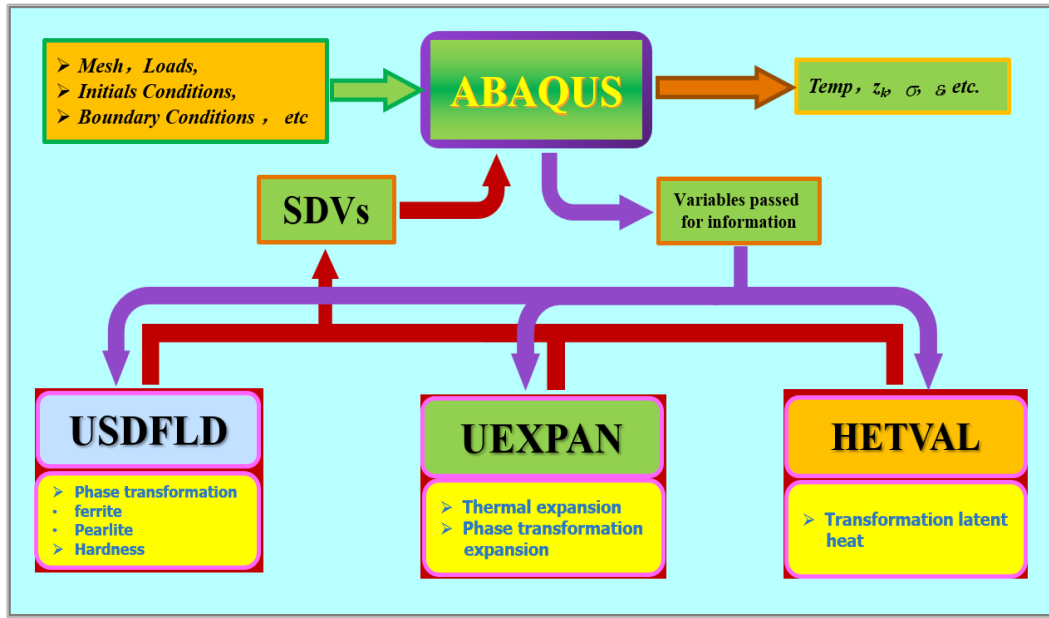


Fig. 6. Schematic diagram of thermo-metallurgical-mechanical coupling model.

The purpose of this study is to reveal the deformation mechanism during the air-cooling of L-beam. The occurrence of a phase change causes a variety of changes in material properties, for example, changes in transformation strain, coefficient of thermal expansion and yield strength. The change in yield strength during cooling was achieved by inputting the high-temperature tensile test data for AH36 steel into ABAQUS software. Three sets of simulation examples were determined by whether or not to consider transformation strain and the change in thermal expansion coefficient due to phase transformation, which was summarized in Table 6. By comparing the calculation results of three sets of examples, the effect of phase change and cooling shrinkage on the deformation of the L-beam can be illustrated. The heat dissipation in the cross-section of an L-beam is much greater than its heat dissipation in the lengthwise direction. The microstructure field is calculated from temperature history data. Therefore,

the paper follows with the analysis of the results for multiple field variables at the cross-sectional position.

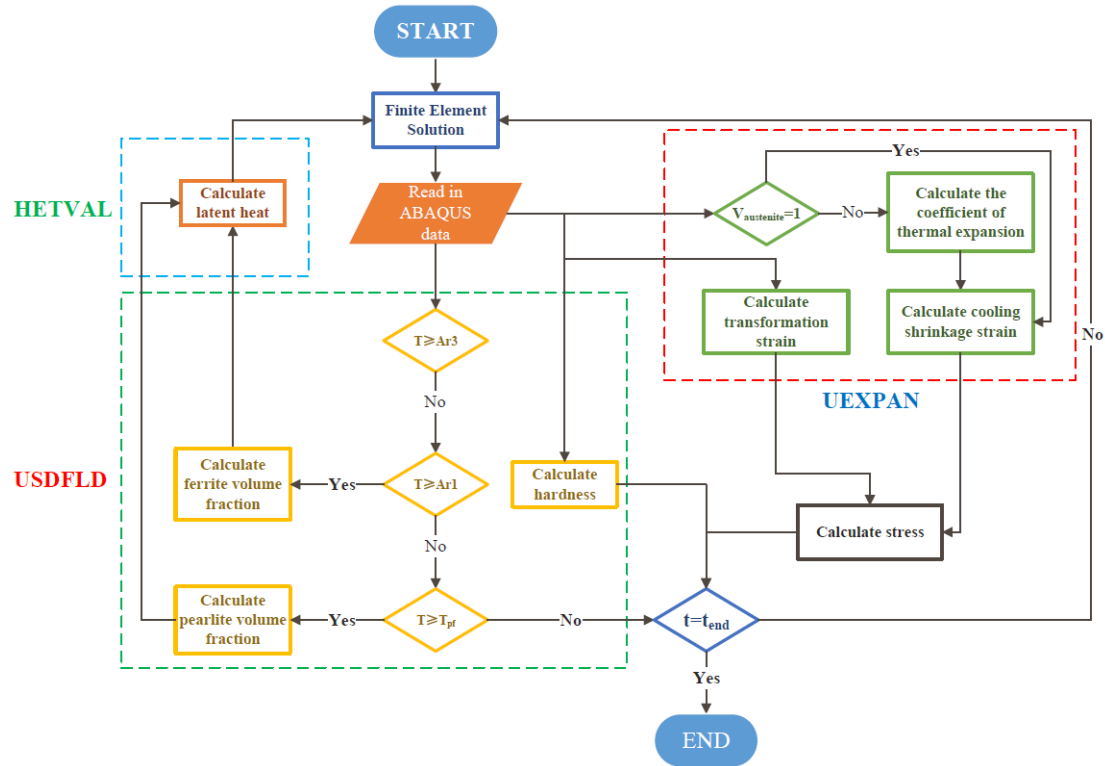


Fig. 7. Calculation flow of the subroutines.

Table 6  
Simulated cases.

Cases	Transformation strain	Change of thermal expansion coefficient
Case A	YES	YES
Case B	No	YES
Case C	No	No

## 4. Results and discussion

### 4.1 Simulated phase transformation

The microstructure of AH36 L-beam under air-cooling is ferrite and pearlite, as shown in Fig. 2. The ferrite and pearlite are formed in the temperature range of 565°C~770°C during the air-cooling process of the L-beam, and the ferrite is formed before the pearlite. This phase transformation temperature interval was measured by a thermal expansion experiment. The fractions of pearlite and ferrite were calculated by the developed USDFLD subroutine based on the temperature history of the nodes. A section of L-beam produced under air-cooling conditions was intercepted to verify the

accuracy of the prepared USDFLD subroutine for the calculation of phase transformation results. The microstructure of the intercepted L-beam was observed and the fraction of microstructure was counted. Samples were taken at six locations on the long edge, short edge and apical horn parts of the L-beam and labeled 1-6, with the sampling locations shown in Fig. 8. The metallographic organization of the six parts was subsequently observed by OM metallographic microscopy and the microstructure fractions were counted by Image-Pro Plus software. The predicted values of the fractions of ferrite and pearlite were compared with the measured statistical values, as shown in Fig. 9. The deviations between the predicted and measured values were within 3%, and the USDFLD subroutine has high accuracy in the calculation of the phase transformation results. In other words, the calculation results of the temperature field also have good accuracy, because the microstructure field was calculated from the temperature history.

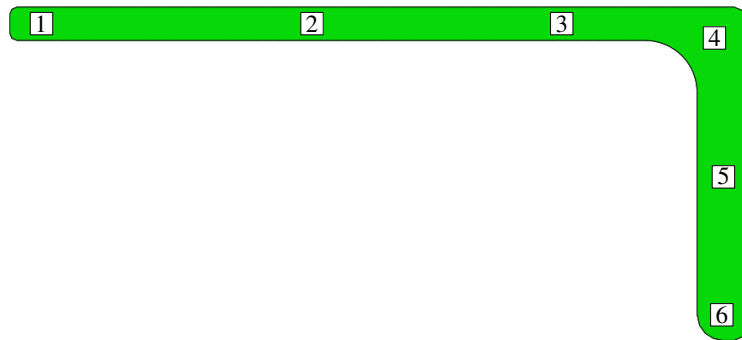


**Fig. 8.** Position of phase fraction statistics on the cross-section of L-beam.

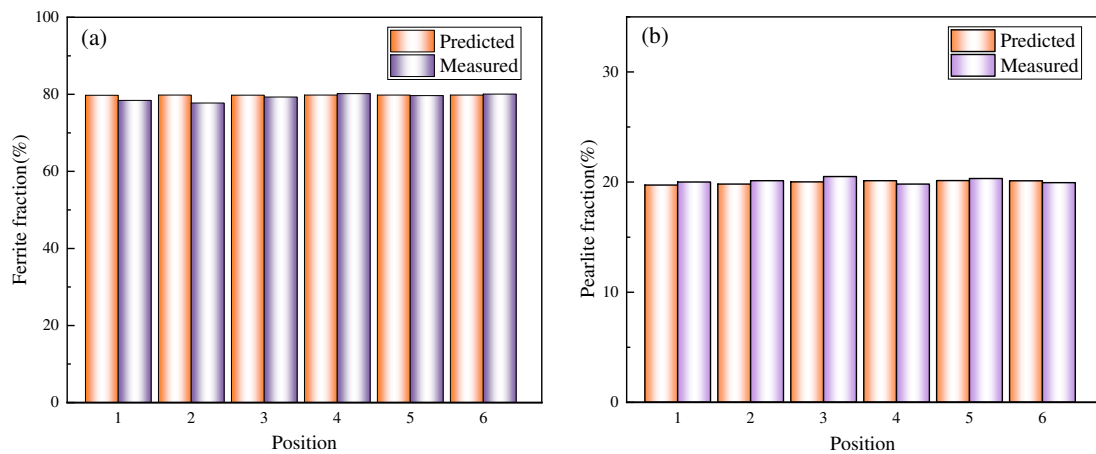


**Fig. 9.** Comparison of predicted and measured values of phase fraction at different locations of the cross-section of L-beam: (a) Ferrite fraction; (b) Pearlite fraction.

The hardness of the six locations shown in Fig. 8 was measured by using the FM-700 microhardness tester. The predicted and measured hardness are presented in Fig. 10. Good agreement is observed between the measured and the predicted hardness values using this model. The distribution of the microstructure determines the hardness. The accuracy of the microstructure calculations is again confirmed.

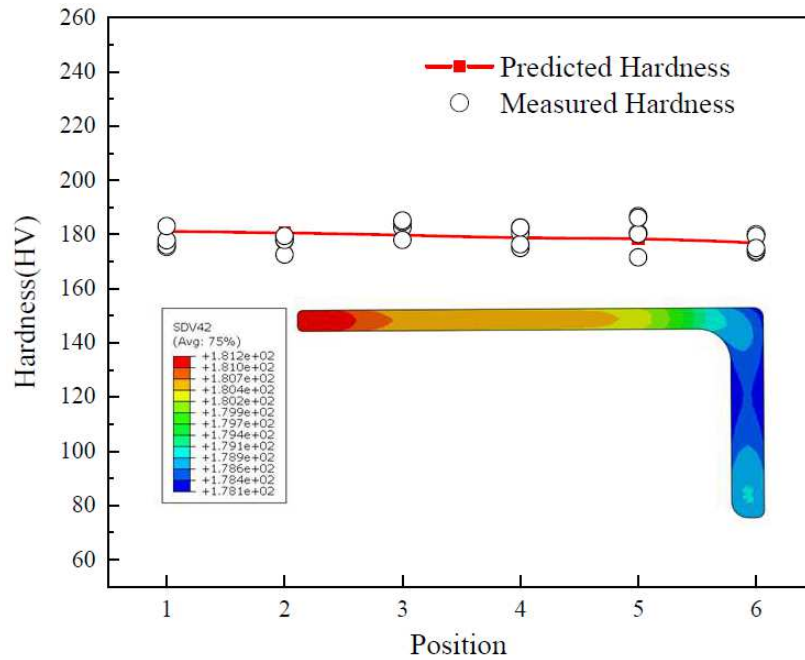


**Fig. 10.** Predicted and measured hardness of the L-beam.

Fig. 11 shows the microstructure distribution contours at the cross-section of the L-beam when the cooling time is 48s, 103s, 173s and 241s. When the cooling time was 48s, the ferrite transformation occurred first due to the lower temperature at the long edge, the ferrite transformation process on the short side was slower than on the long edge, at this time the L-beam did not occur pearlite transformation. When the cooling time was 103s, the ferrite transformation of the long edge was completed, and the ferrite transformation at the short edge was still not completed due to the high temperature. At this time, the pearlite transformation occurred first on the long edge. When the cooling time was 173s, the phase transformation of the long edge was completed, and the ferrite and pearlite transformation was going on at the short edge at the same time because of the high-temperature region at the short edge. As the cooling continues, the ferrite transformation and pearlite transformation of the short

edge were completed one after another, at which time the phase transformation process of the L-beam was completed, and the microstructure distribution of its cross-section is shown in Fig. 11 (g)(h).

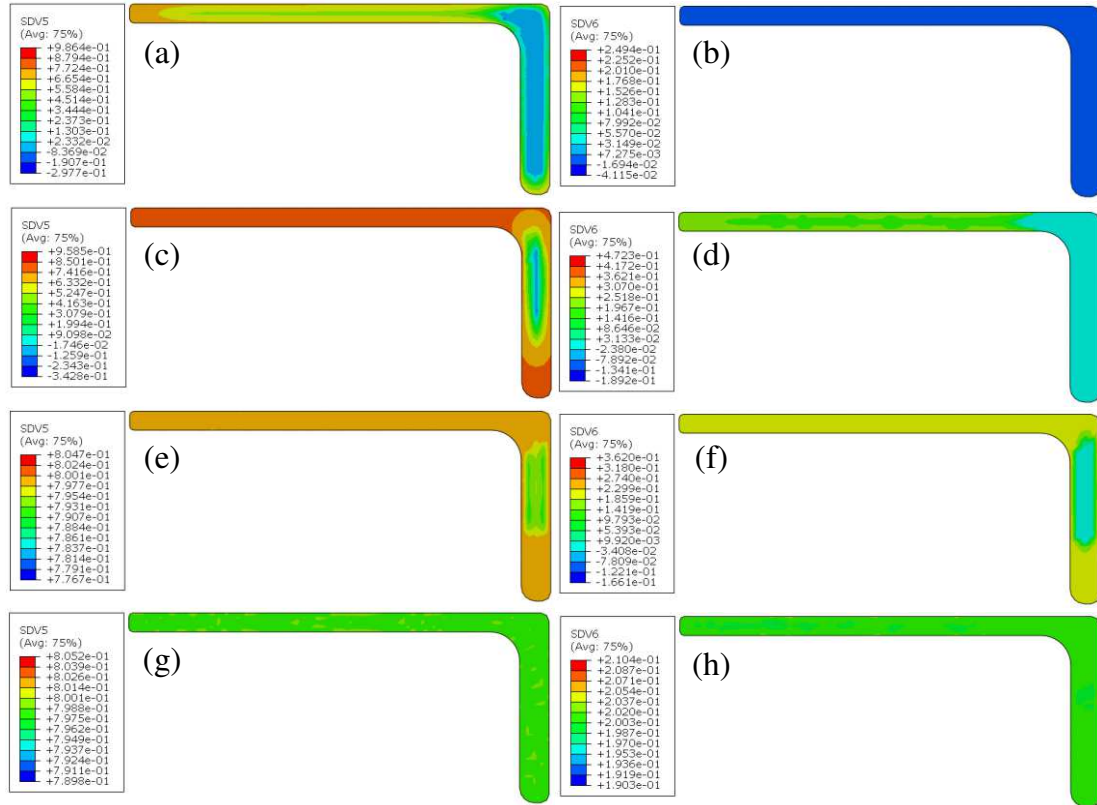


**Fig. 11.** Microstructure distribution contours at different moments during air-cooling: (a) Distribution of ferrite at 48s; (b) Distribution of pearlite at 48s; (c) Distribution of ferrite at 103s; (d) Distribution of pearlite at 103s; (e) Distribution of ferrite at 173s; (f) Distribution of pearlite at 173s; (g) Distribution of ferrite at 241s; (h) Distribution of pearlite at 241s.

Due to the difference in heat dissipation during air-cooling caused by the structural characteristics of the L-beam, the phase transformation process at the long edge precedes that at the short edge, and the degree and type of phase transformation may be different at each part of the cross-section of L-beam at the same moment, indicating that the phase transformation of L-beam during air-cooling has serious non-simultaneous and non-uniformity. Taking a point from each of the long edge and short edge of the L-beam, the curves of the microstructure fractions of the two points with time were shown in Fig. 12. The start time of phase transformation of ferrite and pearlite at the two locations was different, which also indicates that the phase transformation of L-beam is not simultaneous on the long edge and short edge.

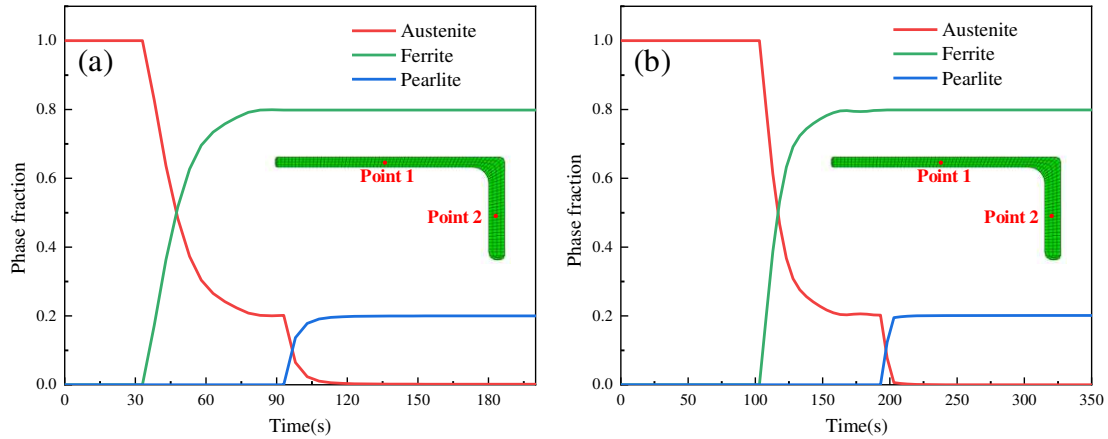


**Fig. 12.** The curves of the microstructure fractions of the two points with time in L-beam section: (a) Curve of point 1; (b) Curve of point 2.

## 4.2 Deformation results

Simulations were performed for each of the three sets of examples in Table 6. Fig. 13 shows the bending state of the L-beam calculated in case A, and the bending order is ① to ③. The three-stage bending of the L-beam in actual production is shown in Fig. 14. From Fig. 13 and Fig. 14, it can be found that the simulated and actual production deformation trends are consistent. The L-beam with bending toward the short edge occurs first during the cooling process, followed by a reversal of the bending direction to the long edge, and finally to the short edge again, with the first stage bending and third stage bending directions consistent. The deformation trend and the deformation sequence of the L-beam in Case B are the same as in Case A, but there is a difference in the degree of deformation.

The final deformation of the L-beam for Case A and Case B compared with the actual measured results as shown in Fig. 15 (c). A positive amount of deformation means that the L-beam is bent to the short edge. Conversely, it indicates bending to the long edge. The calculated results for Case A are closer to the actual measured values, while the deformation results for Case B are more different. The deformation amount at 48s and 220s of Case A and Case B were also compared, and the deformation amount is shown in Fig. 15 (a) (b). From Fig. 15, it can be seen that the results of Case A and Case B differ only in the deformation amount. The simulation results of Case C differ greatly from the actual deformation results, and there are only

two deformation trends ②-③ in Case A. The results of the three sets of simulations show that the calculation results of the model are more accurate when the change in phase transformation strain and expansion coefficient are considered simultaneously, in other words, when the effect of phase transformation is considered. The change in the thermal expansion coefficient of the material induced by the phase transformation affects the deformation tendency of the L-beam, while the transformation strain induced by the phase transformation only affects the amount of deformation. The change of heat transfer coefficient directly affects the cooling shrinkage strain during the cooling process of the L-beam, and the subsequent analysis of the effect of both on the three-stage deformation of the L-beam from the perspective of transformation strain and cooling shrinkage strain.

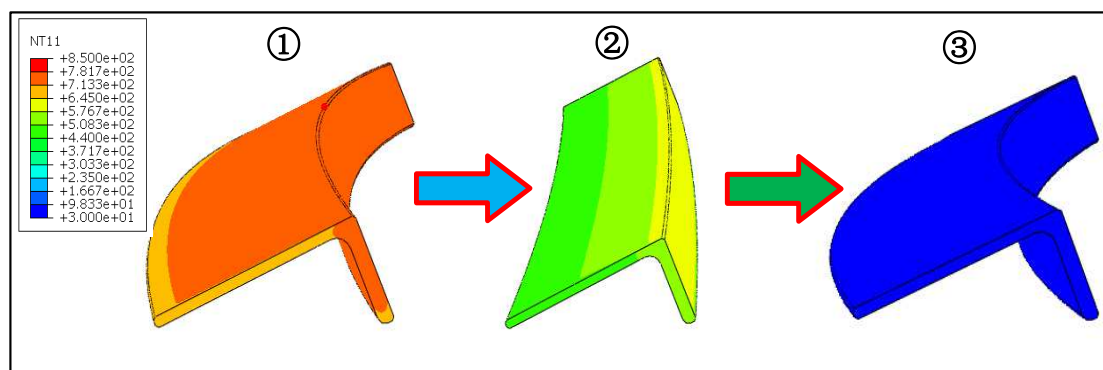


**Fig. 13.** Deformation results for the L-beam in Case A

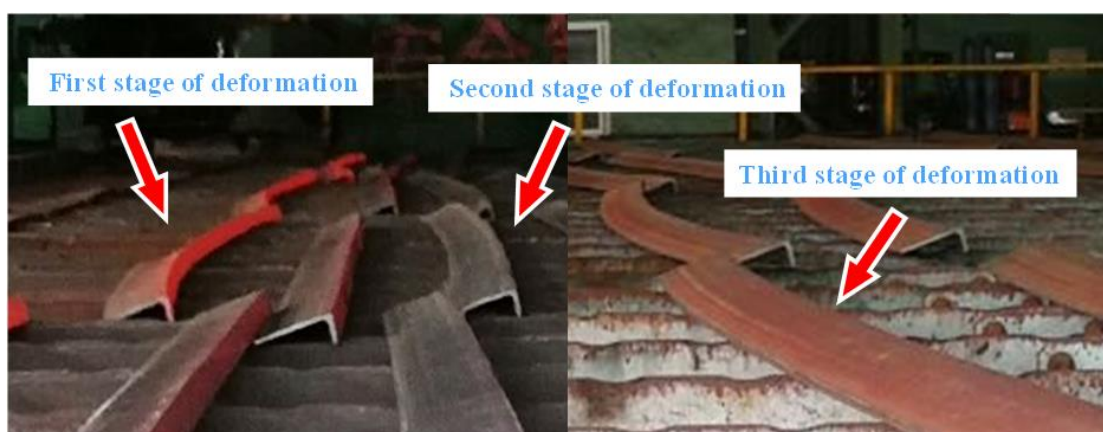


**Fig. 14.** Bending of L-beams in the actual production process.

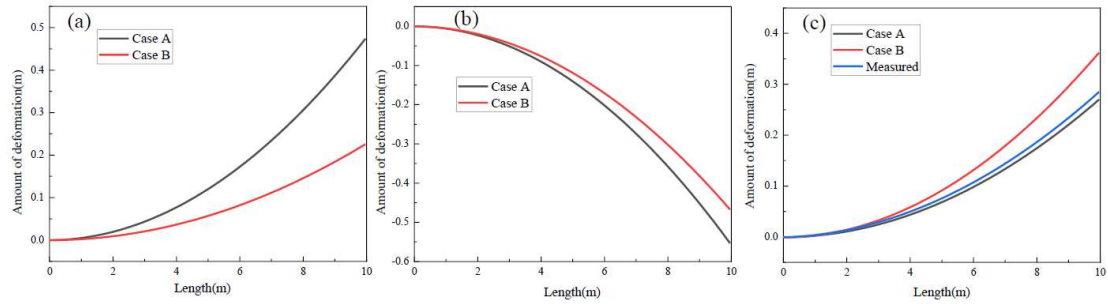


**Fig. 15.** The amount of deformation of L-beam: (a) Comparison of deformation at 48s; (b) Comparison of deformation at 220s; (c) Comparison of final deformations.

Fig.16 shows the distribution clouds of the transformation strain and cooling shrinkage strain for cooling times of 48s, 220s and at the end of cooling. In order to compare more intuitively the magnitude of transformation strain and shrinkage strain at the long edge and short edge of L-beam, the strain results were extracted for the surface layer, 1/4 thickness position and 1/2 thickness position of L-beam, as shown in Fig.17. It can be seen from Fig.17 (a) (d) that when the cooling time is 48s, the temperature of the long edge of the L-beam cools down to the phase transformation temperature firstly, then the phase transformation occurred at the long edge and generated volume expansion, at which time the cooling shrinkage strain of the short edge was larger than that of the long edge, in which the transformation strain and the cooling shrinkage strain together cause the L-beam to show a tendency to bend toward the short edge. The bending deformation of L-beam in the first stage is caused by the superposition of transformation strain and cooling shrinkage strain. During the subsequent cooling process, the short side of the L-beam also begins to undergo phase transformation and the transformation strain on the short edge gradually increases. When the cooling time is 220s, the cooling shrinkage strain on the long edge is greater than that on the short edge, as shown in Fig. 17 (e). And the second stage of bending deformation of the L-beam is also caused by the phase expansion strain and cooling shrinkage strain. When the phase transformation is finished, the phase expansion strain no longer changes, while the cooling contraction strain of the short edge again exceeds that of the long edge, and the cooling contraction strain will keep this trend until the end of cooling, as shown in Fig.17 (c)(f). The bending deformation in the third stage of L-beam is caused by the cooling contraction effect.

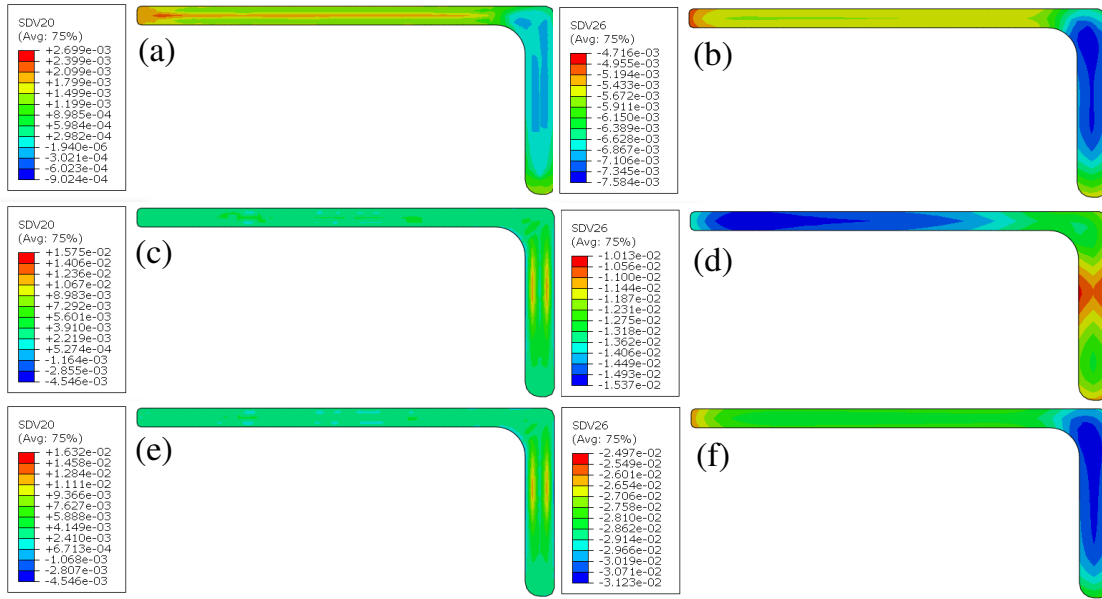


**Fig.16.** Transformation strain and cooling shrinkage strain at different times: (a) Transformation strain at 48s; (b) Cooling shrinkage strain at 48s; (c) Transformation strain at 220s; (d) Cooling shrinkage strain at 220s; (e) The final Transformation Strain; (f) The final Cooling shrinkage strain.

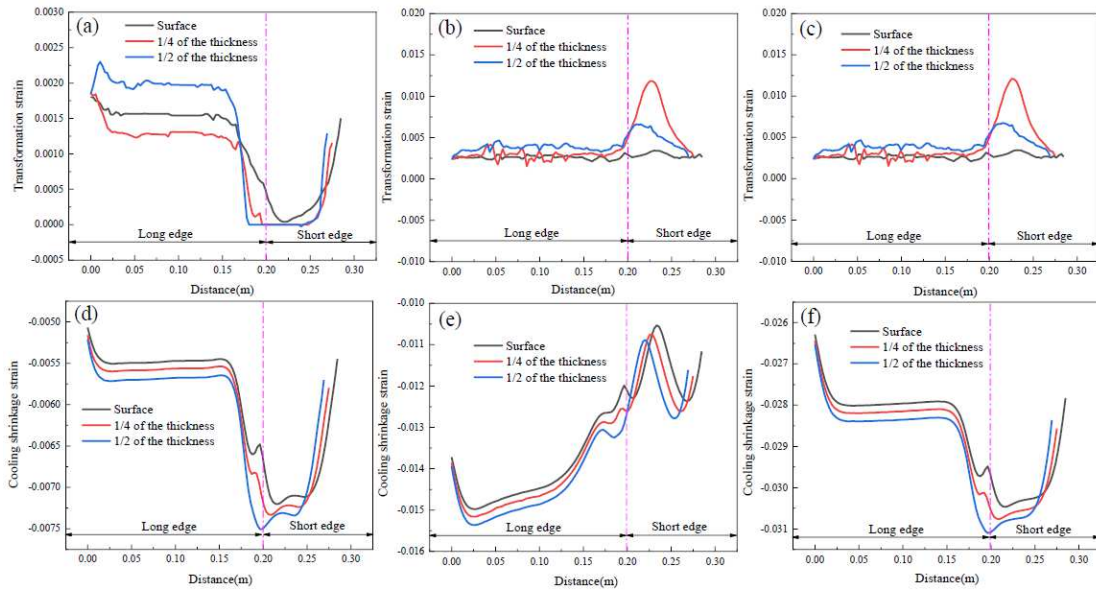


**Fig.17.** Transformation strain and cooling shrinkage strain at different thicknesses of L-beam: (a) Transformation strain at 48s; (b) Transformation strain at 220s; (c) The final Transformation Strain; (d) Shrinkage strain at 48s; (e) Shrinkage strain at 220s; (f) The final shrinkage strain.

Four points were taken in the cross-section of the L-beam, and the curves of the sum of transformation strain and cooling shrinkage strain (thermal strain) at the four points with time are shown in Fig. 18. The repeated variation of the sum of transformation strain and cooling shrinkage strain on the long edge and short edge corresponds to the three-stage bending deformation of the L-beam. The bending

deformation of the L-beam shows a tendency for three-stage bending due to repeated changes in the sum of transformation strain and cooling shrinkage strain.

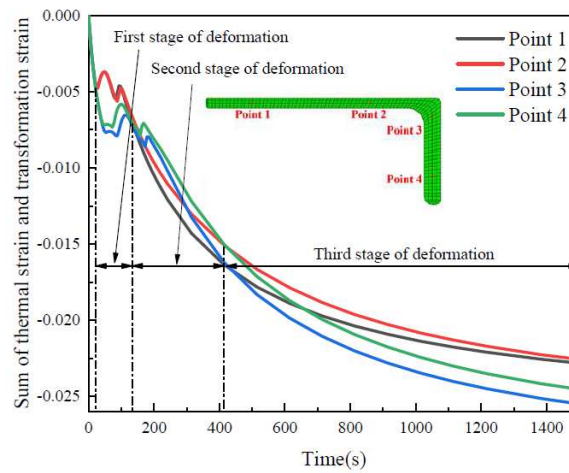


**Fig. 18.** The relationship between the sum of thermal strain and transformation strain with time

### 4.3 Stress distribution analysis

The simulated deformation results of the L-beam in Case A are in good agreement with the actual deformation. If the simulated results have similar deformation to the actual results, the L-beam should also have a similar stress distribution state inside. There were three components of stress in the L-beam according to different directions, S11 (perpendicular to the short side direction), S22 (perpendicular to the long side direction), and S33 (length direction of the L-beam). The stress was extracted from the Line1 position shown in Fig. 19 when the bending deformation occurred, and the stress distribution is shown in Fig. 20. In the process of three deformations, the stress components perpendicular to the short edge and long edge at the position of Line1 did not change significantly, while the stress components along the length of the L-beam changed more significantly.

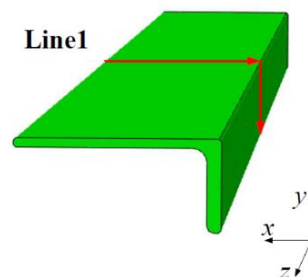


**Fig. 19.** Schematic diagram of L-beam stress extraction location.

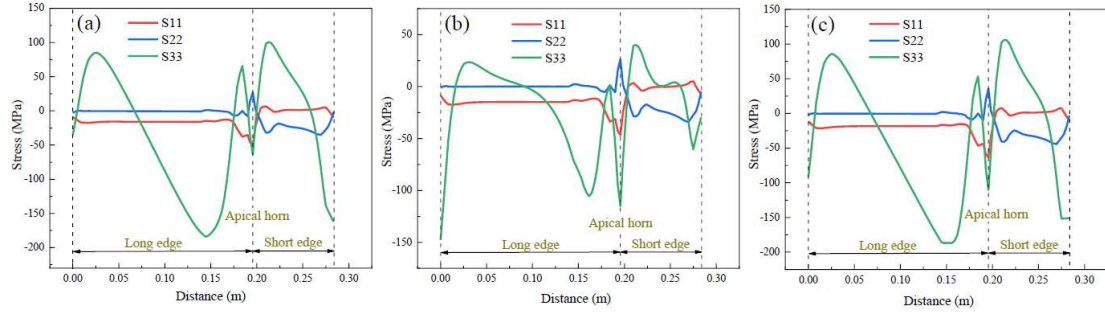


**Fig. 20.** Stress distribution at Line1 of L-beam at three stages of deformation: (a) First stage of deformation; (b) Second stage of deformation; (c) Third stage of deformation.

The stress distribution at the first stage deformation was shown in Fig. 20 (a), the peak tensile stress at the long edge was 85.3 MPa, the peak compressive stress was 184 MPa, and there was a sudden change of stress at the apical horn, the peak tensile stress at the short edge was 100.5 MPa, the peak compressive stress was 162.3 MPa. During the second stage deformation, the stress state was changed. The compressive stress increased sharply at the edge of the long side, the peak stress decreased at other locations, and the nature of the tensile and compressive genus of stress changed at some locations. At the third stage deformation, the stress distribution state was basically the same as that at the first stage deformation. The same deformation trend in L-beam has a similar stress distribution. When the stress state changes, the deformation state of the L-beam also changes.

## 5. Conclusion

In this study, the temperature, microstructure, hardness, deformation, strain and stress during air cooling of the AH36 L-beam were calculated by a coupled thermal-metallurgical-mechanical finite element model using ABAQUS software and subroutines. The accuracy of the microstructure prediction was verified experimentally. The deformation of the L-beam obtained from the simulations is in good agreement with the actual deformation. By comparing the results of three sets of simulation examples and analyzing the results, we can obtain the following conclusions.

(1) The phase transformation process of the L-beam in the air-cooling process is non-uniform and non-simultaneous due to the existence of a temperature gradient. The

calculated results of the phase transformation model were verified by counting the fraction of microstructure and hardness in the cross-section of the L-beam.

(2) The transformation strain caused by the phase change only affects the deformation amount of the three stages of bending deformation of the L-beam, while the change of thermal expansion coefficient caused by the phase transformation affects the bending deformation trend of the L-beam. Considering the effect of phase transformation can significantly improve the calculation accuracy of the model.

(3) The change of the coefficient of thermal expansion directly affects the cooling shrinkage strain during the cooling of the L-beam. The causes of the three-stage deformation of the L-beam are analyzed from the perspective of transformation strain and cooling shrinkage strain. The first stage of bending deformation is caused by the superposition of transformation expansion strain and cooling contraction strain. The second stage of bending deformation is also caused by the effect of transformation expansion strain and cooling contraction strain. The cooling contraction strain is the cause of the third stage of bending deformation.

(4) The stress components along the length of the L-beam change more significantly during the three-stage bending process. the bending deformation trend of the L-beam changes and the stress state also changes. The deformation in the first stage and the deformation in the third stage have similar deformation trends and stress distribution states. From the stress point of view, the three-stage deformation of the L-beam is caused by the stresses induced by the combined effect of transformation strain and cooling contraction strain.

**Funding** This research was financially supported by the National Key Research and Development Program of China (Grant No. 2021YFB3401003).

**Author contribution** Conceptualization, experiment, and article writing were done by Jie Li, numerical simulations by Jie Li and Xianming Zhao, review of paper by Dezhi Li, analysis of numerical simulation by Jie Li and Yang Yang. Discussion of results by Jie Li.

**Data availability** Measurements and simulations data are not publicly available.

**Code availability** The ABAQUS user subroutines written in this study are not publicly available.

## Declarations

**Ethics approval** The authors claim that there are no ethical issues involved in this research.

**Consent to participate** All the authors consent to participate in this research and contribute to the research.

**Consent for publication** All the authors consent to publish the research. There are no potential copyright/plagiarism issues involved in this research.

**Conflict of interest** The authors declare no competing interests.

## References

- [1] K. Zhang, W. Dong, S. Lu, Finite element and experiment analysis of welding residual stress in S355J2 steel considering the bainite transformation, *J. Manuf. Process.* 62 (2021) 80-89, <https://doi.org/10.1016/j.jmapro.2020.12.029>.
- [2] B. Guan, Y. Zang, D. Wu, Q. Qin, Stress-inheriting behavior of H-beam during roller straightening process, *J. Mater. Process. Technol.* 244 (2017) 253-272, <https://doi.org/10.1016/j.jmatprotec.2017.01.026>.
- [3] Z. Liu, Y. Wang, H. Ou, X. Yan, Y. Luo, An analytical leveling model of curvature and residual stress simulation for H-beams, *J. Constr. Steel. Res.* 102 (2014) 13-23, <https://doi.org/10.1016/j.jcsr.2014.06.010>.
- [4] E.V. Zaretsky, Rolling bearing steels – a technical and historical perspective, *Mater. Sci. Technol.* 28 (2013) 58-69, <https://doi.org/10.1179/1743284711Y.0000000043>.
- [5] J. Vaara, A. Kunnari, T. Frondelius, Literature review of fatigue assessment methods in residual stressed state, *Eng. Fail. Anal.* 110 (2020) 104379, <https://doi.org/10.1016/j.engfailanal.2020.104379>.
- [6] F. Wang, X. Men, Y. Liu, X. Fu, Experiment and simulation study on influence of ultrasonic rolling parameters on residual stress of Ti-6Al-4V alloy, *Simul. Model. Pract. Theory.* 104 (2020) 102499, <https://doi.org/10.1016/j.simpat.2020.102121>.

- [7] Z. Ding, G. Sun, M. Guo, X. Jiang, B. Li, S.Y. Liang, Effect of phase transition on micro-grinding-induced residual stress, *J. Mater. Process. Technol.* 281 (2020) 116647, <https://doi.org/10.1016/j.jmatprotec.2020.116647>.
- [8] S. Masoudi, S. Amini, E. Saeidi, H. Eslami-Chalander, Effect of machining-induced residual stress on the distortion of thin-walled parts, *Int. J. Adv. Manuf. Technol.* 76 (2014) 597-608, <https://doi.org/10.1007/s00170-014-6281-x>.
- [9] M. Yaakoubi, M. Kchaou, F. Dammak, Simulation of the thermomechanical and metallurgical behavior of steels by using ABAQUS software, *Comput. Mater. Sci.* 68 (2013) 297-306, <https://doi.org/10.1016/j.commatsci.2012.10.001>.
- [10] A.H. Yaghi, T.H. Hyde, A.A. Becker, W. Sun, Numerical simulation of P91 pipe welding including the effects of solid-state phase transformation on residual stresses, *Proc. Inst. Mech. Eng. Pt. L-J. Mater.-Design Appl.* 221 (2007) 213-224, <https://doi.org/10.1243/14644207JMDA152>.
- [11] S. Phadke, P. Pauskar, R. Shivpuri, Computational modeling of phase transformations and mechanical properties during the cooling of hot rolled rod, *J. Mater. Process. Technol.* 150 (2004) 107-115, <https://doi.org/10.1016/j.jmatprotec.2004.01.027>.
- [12] J.-H. Kim, C.-S. Lee, M.-H. Kim, J.-M. Lee, Prestrain-dependent viscoplastic damage model for austenitic stainless steel and implementation to ABAQUS user-defined material subroutine, *Comput. Mater. Sci.* 67 (2013) 273-281, <https://doi.org/10.1016/j.commatsci.2012.08.021>.
- [13] S. Atlati, B. Haddag, M. Nouari, M. Zenasni, Thermomechanical modelling of the tool-workmaterial interface in machining and its implementation using the ABAQUS VUINTER subroutine, *Int. J. Mech. Sci.* 87 (2014) 102-117, <https://doi.org/10.1016/j.ijmecsci.2014.05.034>.
- [14] S.-K. Kim, C.-S. Lee, J.-H. Kim, M.-H. Kim, J.-M. Lee, Computational evaluation of resistance of fracture capacity for SUS304L of liquefied natural gas insulation system under cryogenic temperatures using ABAQUS user-defined material subroutine, *Mater. Des.* 50 (2013) 522-532, <https://doi.org/10.1016/j.matdes.2013.03.064>.
- [15] C. Şimşir, C.H. Gür, 3D FEM simulation of steel quenching and investigation of the effect of asymmetric geometry on residual stress distribution, *J. Mater. Process. Technol.* 207 (2008) 211-221, <https://doi.org/10.1016/j.jmatprotec.2007.12.074>.
- [16] C.J. Hamelin, O. Muránsky, M.C. Smith, T.M. Holden, V. Luzin, P.J. Bendeich, L. Edwards,

Validation of a numerical model used to predict phase distribution and residual stress in ferritic steel weldments, *Acta Mater.* 75 (2014) 1-19, <https://doi.org/10.1016/j.actamat.2014.04.045>.

[17] C.-H. Lee, K.-H. Chang, Prediction of residual stresses in high strength carbon steel pipe weld considering solid-state phase transformation effects, *Comput. Struct.* 89 (2011) 256-265, <https://doi.org/10.1016/j.compstruc.2010.10.005>.

[18] D. Deng, S. Kiyoshima, Numerical simulation of residual stresses induced by laser beam welding in a SUS316 stainless steel pipe with considering initial residual stress influences, *Nucl. Eng. Des.* 240 (2010) 688-696, <https://doi.org/10.1016/j.nucengdes.2009.11.049>.

[19] D. Deng, H. Murakawa, Influence of transformation induced plasticity on simulated results of welding residual stress in low temperature transformation steel, *Comput. Mater. Sci.* 78 (2013) 55-62, <https://doi.org/10.1016/j.commatsci.2013.05.023>.

[20] B. Kumar, S. Bag, Phase transformation effect in distortion and residual stress of thin-sheet laser welded Ti-alloy, *Opt. Lasers Eng.* 122 (2019) 209-224, <https://doi.org/10.1016/j.optlaseng.2019.06.008>.

[21] Z. Li, S. Yang, B. Liu, W. Liu, Z. Kuai, Y. Nie, Simulation of temperature field and stress field of selective laser melting of multi-layer metal powder, *Opt. Lasers Eng.* 140 (2021) 106782, <https://doi.org/10.1016/j.optlastec.2020.106782>.

[22] Q.H. Zhang, Y. Ma, C. Cui, X.-y. Chai, S.-h. Han, Experimental investigation and numerical simulation on welding residual stress of innovative double-side welded rib-to-deck joints of orthotropic steel decks, *J. Constr. Steel. Res.* 179 (2021) 106544, <https://doi.org/10.1016/j.jcsr.2021.106544>.

[23] W.P. de Oliveira, M.A. Savi, P.M.C.L. Pacheco, L.F.G. de Souza, Thermomechanical analysis of steel cylinders quenching using a constitutive model with diffusional and non-diffusional phase transformations, *Mech. Mater.* 42 (2010) 31-43, <https://doi.org/10.1016/j.mechmat.2009.09.006>.

[24] N.S. Bailey, W. Tan, Y.C. Shin, Predictive modeling and experimental results for residual stresses in laser hardening of AISI 4140 steel by a high power diode laser, *Surf. Coat. Technol.* 203 (2009) 2003-2012, <https://doi.org/10.1016/j.surfcoat.2009.01.039>.

[25] A.K. Esfahani, M. Babaei, S. Sarrami-Foroushani, A numerical model coupling phase transformation to predict microstructure evolution and residual stress during quenching of 1045 steel, *Math. Comput. Simul.* 179 (2021) 1-22, <https://doi.org/10.1016/j.matcom.2020.07.016>.

- [26] M. Kulakov, W.J. Poole, M. Militzer, The Effect of the Initial Microstructure on Recrystallization and Austenite Formation in a DP600 Steel, *Metall. Mater. Trans. A-Phys. Metall. Mater. Sci.* 44 (2013) 3564-3576, <https://doi.org/10.1007/s11661-013-1721-z>.
- [27] S.H. Mohamadi Azghandi, V. Ghanooni Ahmadabadi, I. Raoofian, F. Fazeli, M. Zare, A. Zabet, H. Reihani, Investigation on decomposition behavior of austenite under continuous cooling in vanadium microalloyed steel (30MSV6), *Mater. Des.* 88 (2015) 751-758, <https://doi.org/10.1016/j.matdes.2015.09.046>.
- [28] D. Hömberg, F.S. Patacchini, K. Sakamoto, J. Zimmer, A revisited Johnson–Mehl–Avrami–Kolmogorov model and the evolution of grain-size distributions in steel, *IMA J. Appl. Math.* 82 (2017) 763-780, <https://doi.org/10.1093/imamat/hxx012>.
- [29] K. Zhang, W. Dong, S. Lu, Transformation plasticity of AF1410 steel and its influences on the welding residual stress and distortion: Experimental and numerical study, *Mater. Sci. Eng. A-Struct. Mater. Prop. Microstruct. Process.* 821 (2021) 141628, <https://doi.org/10.1016/j.msea.2021.141628>.
- [30] H. Zhong, Z. Wang, J. Gan, X. Wang, Y. Yang, J. He, T. Wei, X. Qin, Numerical simulation of martensitic transformation plasticity of 42CrMo steel based on spot continual induction hardening model, *Surf. Coat. Technol.* 385 (2020) 125428, <https://doi.org/10.1016/j.surfcoat.2020.125428>.
- [31] M. V. Li, D. V. Niebuhr, L. L. Meekisho, A computational model for the prediction of steel hardenability, *Metall. Mater. Trans. B-Proc. Metall. Mater. Proc. Sci.* 29 (1998) 661-672, <https://doi.org/10.1007/s11663-998-0101-3>.
- [32] J. Sun, T. Nitschke-Pagel, K. Dilger, Influence of temperature- and phase-dependent yield strength on residual stresses in ultra-high strength steel S960 weldments, *J. Mater. Res. Technol.-JMRT.* 15 (2021) 1854-1872, <https://doi.org/10.1016/j.jmrt.2021.09.050>.
- [33] J. Wu, B. Qiang, X. Liao, L. Kang, C. Yao, Y. Li, Experimental investigation and numerical simulation of welding residual stress in orthotropic steel deck with diaphragm considering solid-state phase transformation, *Eng. Struct.* 250 (2022) 113415, <https://doi.org/10.1016/j.engstruct.2021.113415>.
- [34] T. Antretter, D. Zhang, E. Parteder, Modelling Transformation Induced Plasticity - an Application to Heavy Steel Plates, *Steel Res. Int.* 81 (2010) 675-680, <https://doi.org/10.1002/srin.201000081>.